Supporting Information for:

Tailorable Indirect to Direct Bandgap Double Perovskites with Bright White-Light Emission: Decoding Chemical Structure using Solid-State NMR

Abhoy Karmakar,[†] Guy M. Bernard,[†] Alkiviathes Meldrum,[‡] Anton O. Oliynyk,[§] and Vladimir K. Michaelis*[,†]

[†]Department of Chemistry, University of Alberta, Edmonton, Alberta T6G 2G2, Canada
[‡]Department of Physics, University of Alberta, Edmonton, Alberta T6G 2E1, Canada
[§]Chemistry and Biochemistry Department, Manhattan College, Riverdale, New York, 10471, USA

*Corresponding Author: vladimir.michaelis@ualberta.ca

EXPERIMENTAL

Materials and Methods:

All starting materials and solvents were purchased from various commercial sources and used without further purification: CsCl (Tecrochem Laboratories Ltd., AB, Canada), $BiCl_3$ (MilliporeSigma, MO, USA), $InCl_3$ (Alfa Inorganics, Inc., MA, USA), $AgNO_3$ (EM Science, Darmstadt, Germany), HCl (Caledon Laboratory Chemicals, ON, Canada). All materials were synthesized and characterized under ambient atmosphere and temperature.

Synthesis of Polycrystalline $Cs_2Bi_{1-x}In_xAgCl_6$ ($0 \leq x \leq 1$) HDPs:

AgCl salt was freshly synthesized by the addition of an excess amount of concentrated HCl to an aqueous solution of $AgNO_3$, resulting in a solid white precipitate. This white solid was filtered with a Buchner funnel, washed with 95% ethanol, and then dried under vacuum filtration. Afterwards, 1 mmol of freshly prepared AgCl in conc. HCl (at *ca.* 120 °C and constant stirring), (1–*x*) mmol of $BiCl_3$ and x mmol of $InCl_3$ were added to the hot conc. HCl solvent within the vial, followed by an addition of 2 mmol of CsCl powder. White (when x = 1.0) to yellow (when x = 0.0) precipitates were observed immediately. The mixtures were heated for an hour with medium stirring and then allowed to stand at room temperature for two more hours. The precipitates were then filtered using a Buchner funnel and washed with 95% washing ethanol. These solid samples were stored in vials under ambient conditions and used for further characterization.

Powder X-ray Diffraction (PXRD):

Powder X-ray diffraction measurements for the polycrystalline solid samples were collected on an Inel MPD multi-purpose diffractometer (40 kV, 50 mA) system equipped with a CPS 120 curved position sensitive X-ray detector and a 1.540596 Å Cu K_α radiation source. All samples were placed on a plastic sample holder and 2θ data from ~ 0° to 113° were collected. The cell constants were determined from the profile fitting of the PXRD patterns using the FullProf Suite software.

Energy-dispersive X-ray spectroscopy (EDS) and Field Emissive Scanning Electron Microscopy (FESEM):

The FESEM measurements were performed using a Zeiss Sigma 300 VP equipped with dual silicon drift detectors for EDS measurements.

Inductively Coupled Plasma Optical Emission Spectroscopy (ICP-OES):

A Thermo iCAP 6000 series ICP-OES spectrometer was used for Bi and In concentration measurements. The samples were dissolved in *aqua regia* and the resultant solution was further diluted with deionized water.

Thermogravimetric Analysis (TGA):

TGA analyses were performed on a Perkin Elmer Pyris 1 Thermogravimetric Analyzer. The samples were heated under an N_2 atmosphere at a heating rate of 5–10 ^{o}C/min from 25–800 ^{o}C.

UV-Vis Diffuse Reflectance (DR) Spectroscopy:

All the UV-Vis diffuse reflectance spectra for the polycrystalline $Cs_2Bi_{1-x}In_xAgCl_6$ double perovskite samples were collected using a Cary 5000 UV−Vis−NIR spectrophotometer. For each sample, a small amount (50 to 100 mg) of powder was packed into a black boat and measurements were obtained at wavelengths between 200 and 800 nm. The instrument was calibrated with a Spectralon (>99%) reflectance standard.

All the DR spectra were converted to pseudo-absorbance spectra using the Kubelka-Munk[1] transformation as follows: $\alpha \sim (1-R)^2/(2R)$, where, R and α are the absolute reflectance and pseudo-absorbance, respectively. The indirect and direct bandgaps were experimentally determined from the intercept values upon extrapolation of the linear regions of $(\alpha h\nu)^{1/2}$ vs E(eV) and $(\alpha h\nu)^2$ vs E(eV) plots, respectively.

Steady-State and Time-Resolved Photoluminescent (PL) Spectroscopy and PLQY:

Photoluminescence spectroscopy was performed using a 365+351 nm Ar ion laser source. A 400-nm longpass filter was used to block the scattered laser light and the spectra were measured with an intensity-calibrated Ocean Optics USB2000 spectrometer. Time-resolved PL measurements were performed using a pulsed laser excitation of 365+351 nm Ar ion laser interfaced to an acousto-optic modulator (~10 ns response time) and a Hamamatsu H7422 PMT.

The PLQY was measured using a Photon Technology International (PTI) MP1 Fluorescence System with a 75 W Xenon arc lamp as an excitation source and equipped with an integrating sphere. Solid $BaSO_4$ was used as a reference sample. Equivalent amounts of sample and reference solids were taken in melting point capillary tubes which were placed in the integrating sphere for further measurements. Samples and the reference were excited at λ_{max} = 370 or 380 nm and emission spectra were collected between 410 to 900 nm, respectively.

Solid-State Nuclear Magnetic Resonance (NMR) Spectroscopy:

(i) Cesium-133 NMR spectroscopy:

(a) Solid-state ^{133}Cs NMR spectra were acquired at 21.14 T (900 MHz, ^{1}H) on a Bruker Avance II 900 spectrometer under magic angle spinning (MAS) conditions using a 2.5 mm H/X MAS Bruker probe with $\gamma B_o/2\pi(^{133}Cs)$ = 118.0 MHz and the sample spinning at a spinning frequency of 30 kHz. All samples were packed into 2.5 mm o.d. ZrO_2 rotors. A Bloch decay pulse sequence was used with a 0.50 μs pulse width (~20° tip angle, $\gamma B_1/2\pi$ (solid) = 111 kHz), an acquisition time of 20 ms, an optimized recycle delay of 90 s (see Figure S18, Table S6) and 32 co-added transients.

(b) Solid-state ^{133}Cs NMR measurements were performed at 11.75 T (500 MHz, ^{1}H) on a Bruker Avance 500 spectrometer under MAS conditions using a 4 mm H/X Bruker MAS probe with $\gamma B_o/2\pi(^{133}Cs)$ = 65.6 MHz and a MAS frequency of 13 kHz. All samples were packed into 4 mm o.d. ZrO_2 rotors. Data were acquired using a Bloch decay pulse (π/2 pulse of 1.25 μs, $\gamma B_1/2\pi$ (solution) = 50.0 kHz), an acquisition time of 50-100 ms, a recycle delay of 300-5000 s and 1-8 co-added transients.

All ^{133}Cs NMR spectra discussed here were referenced by setting the ^{133}Cs NMR peak of a 0.1 M CsCl aqueous solution to δ = 0.0 ppm.

(ii) Bismuth-209 NMR spectroscopy:

(a) Solid-state ^{209}Bi NMR spectra were acquired at 21.14 T (900 MHz, ^{1}H) on the Bruker Avance II 900 spectrometer. Non-spinning ^{209}Bi NMR spectra were collected using a 4 mm H/X MAS Bruker probe with $\gamma B_o/2\pi(^{209}Bi)$ = 145 MHz. Samples were packed in 4 mm thick-walled Bruker o.d. ZrO_2 rotors and a modified quadrupolar-echo pulse sequence[2,3] ($(\pi/2)_x - \tau_1 - (\pi/2)_y - \tau_2 - ACQ$), where τ_1 and τ_2 represent the inter-pulse and refocusing delays, respectively) was used to achieve broader excitation width and minimize line distortions at higher magnetic field strengths with a solid 1.0 μs π/2 pulses ($\gamma B_1/2\pi$ (solution) = 50 kHz). An echo delay of 20 μs was used for all the measurements. A recycle delay of 0.5 s and 16,000 to 80,000 co-added transients were used for each non-spinning ^{209}Bi NMR measurement.

Magic-angle spinning ^{209}Bi NMR spectra were collected using a 2.5 mm H/X MAS Bruker probe with $\gamma B_o/2\pi(^{209}Bi)$ = 145 MHz with magic-angle spinning frequency of 30 kHz. The spectra were acquired using either a Bloch decay pulse of 0.2 μs (short tip angle ~ 20° solid) or a modified rotor-synchronized quadrupolar-echo pulse sequence[2,3] ($(\pi/2)_x - \tau_1 - (\pi/2)_y - \tau_2 - ACQ$), where τ_1

and τ_2 represent the inter-pulse and refocusing delays), with a 0.5 μs π/2 pulses ($\gamma B_1/2\pi$ (solution) = 100 kHz). An echo delay of 33 μs was used for rotor-synchronized quadrupolar-echo experiments. A recycle delay of 0.5 s and 1,000-48,000 co-added transients were used for each ^{209}Bi MAS NMR measurement.

(b) An additional ^{209}Bi NMR measurements for $Cs_2BiAgCl_6$ parent material were performed at 7.05 T (300 MHz, ^{1}H) and 11.75 T (500 MHz, ^{1}H) on a Bruker Avance 300 and 500 spectrometers with $\gamma B_o/2\pi(^{209}Bi)$ = 48.5 and 80.7 MHz, respectively, using a 4 mm H/X Bruker MAS probe. Samples were packed in 4 mm o.d. ZrO_2 rotors and magic-angle spinning (MAS = 10 kHz) spectra were acquired using a Bloch decay pulse of 1 μs (solid π/2; $\gamma B_1/2\pi$ (solution) = 50 kHz) and non-spinning spectra were acquired using a Hahn-echo pulse sequence ($(\pi/2)_x - \tau_1 - (\pi)_y - \tau_2 -$ ACQ), where τ_1 and τ_2 represent the inter-pulse and refocusing delays), with a 1.0 μs π/2 pulses ($\gamma B_1/2\pi$ = 50 kHz). An echo delay of 40 μs and recycle delay of 0.2-1.0 s were used.

All ^{209}Bi NMR spectra discussed above were referenced using saturated $Bi(NO_3)_3$ in a concentrated HNO_3 solution to set the ^{209}Bi peak at δ = 0.0 ppm.

(iii) Indium-115 NMR spectroscopy:

Solid-state ^{115}In NMR spectra were acquired at 21.14 T (900 MHz, ^{1}H) on the Bruker Avance II 900 spectrometer with the 4 mm H/X MAS Bruker probe with $\gamma B_o/2\pi(^{115}In)$ = 197.1 MHz, using either a Bloch decay pulse of 0.2 μs (short tip angle ~ 20° solid) or a modified quadrupolar-echo pulse sequence[2,3] ($(\pi/2)_x - \tau_1 - (\pi/2)_y - \tau_2 -$ ACQ), where τ_1 and τ_2 represent the inter-pulse and refocusing delays), with a solid 1.0 μs π/2 pulses ($\gamma B_1/2\pi$ (solution) = 50 kHz). ^{115}In MAS NMR spectra were acquired using the Bloch decay pulse and a spinning frequency of 18 kHz. Non-spinning ^{115}In NMR data were acquired using the quadrupolar-echo pulse sequence with an echo delay of 20 μs and 4,000-40,000 co-added transients. A recycle delay of 1 s was used for all the measurements.

An additional ^{115}In NMR measurements for $Cs_2InAgCl_6$ parent material were performed at 11.75 T (500 MHz, ^{1}H) on a Bruker Avance 500 spectrometers with $\gamma B_o/2\pi(^{115}In)$ = 109.6 MHz, using a 4 mm H/X Bruker MAS probe. Samples were packed in 4 mm o.d. ZrO_2 rotors and magic-angle spinning (MAS = 10 kHz) spectra were acquired using a Bloch decay pulse of 0.7 μs (solid π/2; $\gamma B_1/2\pi$ (solution) = 71.4 kHz) and non-spinning spectra were acquired using a solid-echo pulse sequence ($(\pi/2)_x - \tau_1 - (\pi/2)_y - \tau_2 -$ ACQ), here τ_1 and τ_2 represent the inter-pulse and refocusing

delays), with a 0.7 μs solid π/2 pulses ($\gamma B_1/2\pi$ = 71.4 kHz). An echo delay of 40 μs and recycle delay of 2.0 s were used.

All ^{115}In NMR spectra were referenced using 0.1 M $In(NO_3)_3$ in 0.5 M HNO_3 to set the ^{115}In peak at δ = 0.0 ppm.

Quantum Chemical Calculations:

(i) Electronic Band Structure Calculations: Five structural models of the $Cs_2Bi_{1-x}In_xAgCl_6$ compounds were used for calculations, with x = 0, 0.25, 0.5, 0.75, and 1. Structure optimization, total energy calculations, band dispersion, density of states, and electron localization function calculations[4–6] were performed with the Vienna Ab Initio Simulation Package (VASP) within the density functional theory framework.[7,8] The electronic wave functions were defined with the plane-wave basis set and projector-augmented wave potentials.[9] The structural optimization electronic convergence criteria were set to 1×10^{-8} eV, and the ionic optimization was set to 1×10^{-2} eV/ Å. A 500 eV plane wave cutoff energy was used and the integration of the first Brillouin zone was carried out using a Monkhorst−Pack k-point grid of 8 × 8 × 8. The HSE06 functional was implemented to estimate the band gap (corrected for the significant underestimation of the Perdew-Bruke-Ernzerhof (PBE) band gap), which resulted in Eg = 2.52 eV and 3.51 eV for $Cs_2BiAgCl_6$ and $Cs_2InAgCl_6$, respectively, which is in a good agreement with the experimental values (2.70 eV and 3.67 eV, respectively). The calculated band gap values were obtained by implementing a mixture of PBE:Hartree−Fock (75:25). To analyse the valence electron charge redistribution, a Bader charge analysis was employed.[10]

(ii) DFT: A series of gauge-including projector-augmented wave (GIPAW) DFT calculations were performed to assess the impact of B'(III)-site substitutions on the ^{209}Bi and ^{115}In electric field gradients (EFG), implemented within version 4.4 of the CASTEP software.[11] Using a primitive symmetry supercell the computed EFGs were obtained on a series of model structures by varying the Bi/In substitutions. All calculations used the PBE functional in the GGA for the exchange-correlation energy[12,13] and ultrasoft pseudopotentials[14] on all-atom geometry-optimized primitive clusters. Calculations were performed with a coarse accuracy basis set and a maximum plane-wave energy of 244.90 eV using an HP xw4400 workstation with a single Intel Dual-Core 2.67 GHz processor and 8 GB RAM. The computed EFGs were converted to quadrupole coupling constants using 0.81 and 0.516 barn for the ^{115}In and ^{209}Bi quadrupolar moments.[15] The DFT calculations were performed on the most symmetric substitutions that could be accommodated with current

hardware that is restricted in handling large unit cell volumes. Therefore, the presented calculations are considered “best-case” symmetric scenarios. The non-symmetric Bi/In substitutions within the 12 possible environments could increase the experimental quadrupolar coupling constants beyond these values. Considering the potential for sizable quadrupole couplings and populations there is the potential for invisible Bi (or In) environments.

Table S1. Elemental analysis of $Cs_2Bi_{1-x}In_xAgCl_6$ mixed-cationic double perovskites measured by EDS and ICP-OES.

Sample (Nominal composition)	Atom% by EDS[a]					Atomic ratio of In : Bi		
	Cs	Bi	In	Ag	Cl	Nominal	EDS	ICP-OES
$Cs_2InAgCl_6$	18.83 (1.15)	-	9.96 (0.89)	9.56 (0.72)	61.65 (1.85)	1.00 : 0.00	1.00 : 0.00	-
$Cs_2Bi_{0.01}In_{0.99}AgCl_6$	19.46 (0.80)	0.00 (0.00)	10.08 (0.34)	9.05 (0.52)	61.40 (1.09)	0.99 : 0.01	1.00 : 0.00	0.981: 0.019
$Cs_2Bi_{0.05}In_{0.95}AgCl_6$	19.20 (0.46)	0.05 (0.04)	9.28 (0.15)	9.71 (0.32)	61.76 (0.82)	0.95 : 0.05	0.99 : 0.01	0.915 : 0.085
$Cs_2Bi_{0.25}In_{0.75}AgCl_6$	18.82 (0.56)	1.65 (0.17)	7.74 (0.29)	9.46 (0.46)	62.33 (1.20)	0.75 : 0.25	0.82 : 0.18	0.78 : 0.22
$Cs_2Bi_{0.35}In_{0.65}AgCl_6$	19.28 (0.36)	2.58 (0.41)	6.65 (0.50)	9.11 (0.69)	62.38 (1.02)	0.65 : 0.35	0.72 : 0.28	0.65 : 0.35
$Cs_2Bi_{0.50}In_{0.50}AgCl_6$	19.98 (0.70)	4.65 (0.45)	4.85 (0.28)	10.48 (1.04)	60.04 (1.90)	0.50 : 0.50	0.51 : 0.49	0.50 : 0.50
$Cs_2Bi_{0.75}In_{0.25}AgCl_6$	19.68 (0.44)	7.06 (0.37)	2.18 (0.29)	10.07 (0.93)	61.00 (0.78)	0.25 : 0.75	0.24 : 0.76	0.28 : 0.72
$Cs_2Bi_{0.95}In_{0.05}AgCl_6$	19.98 (1.21)	8.87 (0.52)	0.33 (0.09)	9.32 (0.54)	61.50 (1.18)	0.05 : 0.95	0.04 : 0.96	0.076 : 0.924
$Cs_2BiAgCl_6$	20.37 (1.75)	10.22 (0.40)	-	9.37 (0.64)	60.03 (1.57)	0.00 : 1.00	0.00 : 1.00	-

a – Standard deviation of EDS measurements based on 5 point measurements.

Table S2. Chemical formula of $Cs_2Bi_{1-x}In_xAgCl_6$ pre- and post-synthesis as determined by EDS and ICP-OES elemental analysis.

Nominal compositions	Chemical composition of the products	
	EDS	ICP-OES
$Cs_2InAgCl_6$	$Cs_2InAgCl_6$	$Cs_2InAgCl_6$
$Cs_2Bi_{0.01}In_{0.99}AgCl_6$	$Cs_2Bi_{0.00}In_{1.00}AgCl_6$	$Cs_2Bi_{0.019}In_{0.981}AgCl_6$
$Cs_2Bi_{0.05}In_{0.95}AgCl_6$	$Cs_2Bi_{0.02}In_{0.98}AgCl_6$	$Cs_2Bi_{0.085}In_{0.915}AgCl_6$
$Cs_2Bi_{0.25}In_{0.75}AgCl_6$	$Cs_2Bi_{0.18}In_{0.82}AgCl_6$	$Cs_2Bi_{0.22}In_{0.78}AgCl_6$
$Cs_2Bi_{0.35}In_{0.65}AgCl_6$	$Cs_2Bi_{0.28}In_{0.72}AgCl_6$	$Cs_2Bi_{0.35}In_{0.65}AgCl_6$
$Cs_2Bi_{0.50}In_{0.50}AgCl_6$	$Cs_2Bi_{0.49}In_{0.51}AgCl_6$	$Cs_2Bi_{0.50}In_{0.50}AgCl_6$
$Cs_2Bi_{0.75}In_{0.25}AgCl_6$	$Cs_2Bi_{0.76}In_{0.24}AgCl_6$	$Cs_2Bi_{0.72}In_{0.28}AgCl_6$
$Cs_2Bi_{0.95}In_{0.05}AgCl_6$	$Cs_2Bi_{0.96}In_{0.04}AgCl_6$	$Cs_2Bi_{0.924}In_{0.076}AgCl_6$
$Cs_2BiAgCl_6$	$Cs_2BiAgCl_6$	$Cs_2BiAgCl_6$

Table S3. Bader charges for the $Cs_2Bi_{1-x}In_xAgCl_6$ series.

In_x	Cs	Bi	In	Ag	Cl
0	+0.8794	+1.6453	N/A	+0.6136	-0.6696
0.25	+0.8838	+1.5053	+1.2798	+0.6034	-0.6367
0.5	+0.8848	+1.4463	+1.2753	+0.5878	-0.6197
0.75	+0.8835	+1.4746	+1.3183	+0.5703	-0.6158
1.0	+0.8815	N/A	+1.8006	+0.5559	-0.6075

Table S4. Mono-, bi-, and stretched exponential fitting parameters of PL decay for $Cs_2Bi_{0.085}In_{0.915}AgCl_6$ and $Cs_2Bi_{0.22}In_{0.78}AgCl_6$ HDPs upon laser excitation of λ_{ex} = 364 nm and λ_{em} = 625 nm.

Sample	**Fitting Model**	**Model Equations** [a]	**Fitted Parameters**	**Reduced χ^2**
$Cs_2Bi_{0.085}In_{0.915}AgCl_6$	Monoexp.	$I = a_1 e^{-t/\tau}$	τ = 662 ± 2 ns	$8.0*10^{-5}$
	Biexp.	$I = a_1 e^{-t/\tau_1} + a_1 e^{-t/\tau_2}$	τ_1 = 279 ± 3 ns (a_1 = 36%) τ_2 = 865 ± 4 ns (a_2 = 64%)	$7.2*10^{-6}$
	Stretched exp.	$I = a_1 e^{-(t/\tau_{SE})^{\beta}}$	τ_{SE} = 571 ± 1 ns β = 0.82	$7.6*10^{-6}$
$Cs_2Bi_{0.22}In_{0.78}AgCl_6$	Monoexp.	$I = a_1 e^{-t/\tau}$	τ = 925 ± 1 ns	$2.4*10^{-5}$
	Biexp.	$I = a_1 e^{-t/\tau_1} + a_1 e^{-t/\tau_2}$	τ_1 = 403± 14 ns (a_1 = 17%) τ_2 = 1022 ± 5 ns (a_2 = 83%)	$9.8*10^{-6}$
	Stretched exp	$I = a_1 e^{-(t/\tau_{SE})^{\beta}}$	τ_{SE} = 883 ± 1 ns β = 0.93	$9.6*10^{-6}$

a – In equations: I = time-dependent luminescence intensity, a = amplitude, t = time, τ = time constant, β = stretching parameter ($0 < \beta < 1$).

Table S5. Biexponential fitting of wavelength dependent PL decay for $Cs_2Bi_{0.085}In_{0.915}AgCl_6$ and $Cs_2Bi_{0.22}In_{0.78}AgCl_6$ HDPs upon laser excitation of λ_{ex} = 364 nm.

Sample	λ_{em}	PL lifetime (τ) and their contribution (a)		Average lifetime,[a] τ_{avg}/ns
		τ_1/ns (a_1)	τ_2/ns (a_2)	
$Cs_2Bi_{0.085}In_{0.915}AgCl_6$	550 nm	250 ± 3 (37%)	834 ± 3 (63%)	746
	625 nm	279 ± 3 (36%)	865 ± 4 (64%)	774
	700 nm	288 ± 4 (35%)	877 ± 4 (65%)	790
$Cs_2Bi_{0.22}In_{0.78}AgCl_6$	550 nm	405 ± 13 (19%)	1027 ± 5 (81%)	976
	625 nm	403 ± 14 (17%)	1022 ± 5 (83%)	978
	700 nm	464 ± 17 (19%)	1058 ± 7 (81%)	1003

[a] Intensity *average lifetime* (τ_{avg}) $= \frac{(a_1\tau_1^2 + a_2\tau_2^2)}{(a_1\tau_1 + a_2\tau_2)}$

Table S6. Spin-lattice relaxation time (T_1) values.
(a) ^{115}In and ^{209}Bi T_1 values at 7.05 T under non-spinning sample conditions.

Sample	T_1(^{115}In)/s	T_1(^{209}Bi)/s
$Cs_2InAgCl_6$	0.0380 ± 0.0003	n.a.
$Cs_2BiAgCl_6$	n.a.	0.0250 ± 0.0004

(b) ^{133}Cs T_1 values at 11.75 T under magic-angle spinning (ν_{rot} =13 kHz) sample condition.

Sample	T_1(^{133}Cs)/s Cuboctahedron sites				
	Site 1 	Site 2 	Site 3 	Site 4 	Site 5 
$Cs_2BiAgCl_6$	157 ± 23	-	-	-	-
$Cs_2Bi_{0.924}In_{0.076}AgCl_6$	235 ± 20	271 ± 26	-	-	-
$Cs_2Bi_{0.50}In_{0.50}AgCl_6$	-	-	548 ± 26	-	-
$Cs_2Bi_{0.085}In_{0.915}AgCl_6$	-	-	-	914 ± 38	920 ± 15
$Cs_2InAgCl_6$	-	-	-		931 ± 5

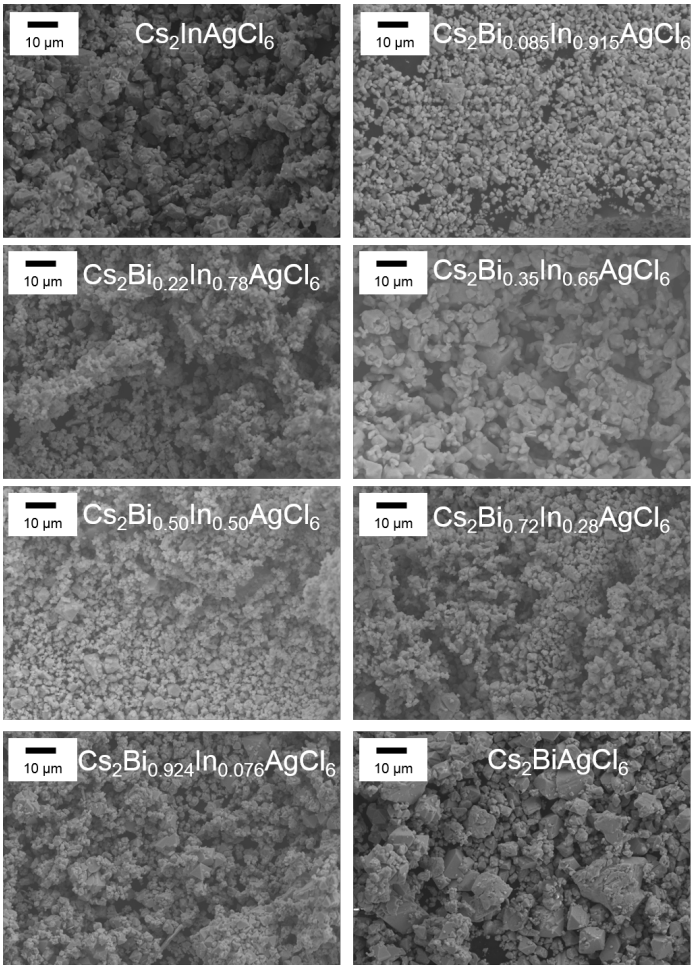

Figure S1. FESEM images of the $Cs_2Bi_{1-x}In_xAgCl_6$ series.

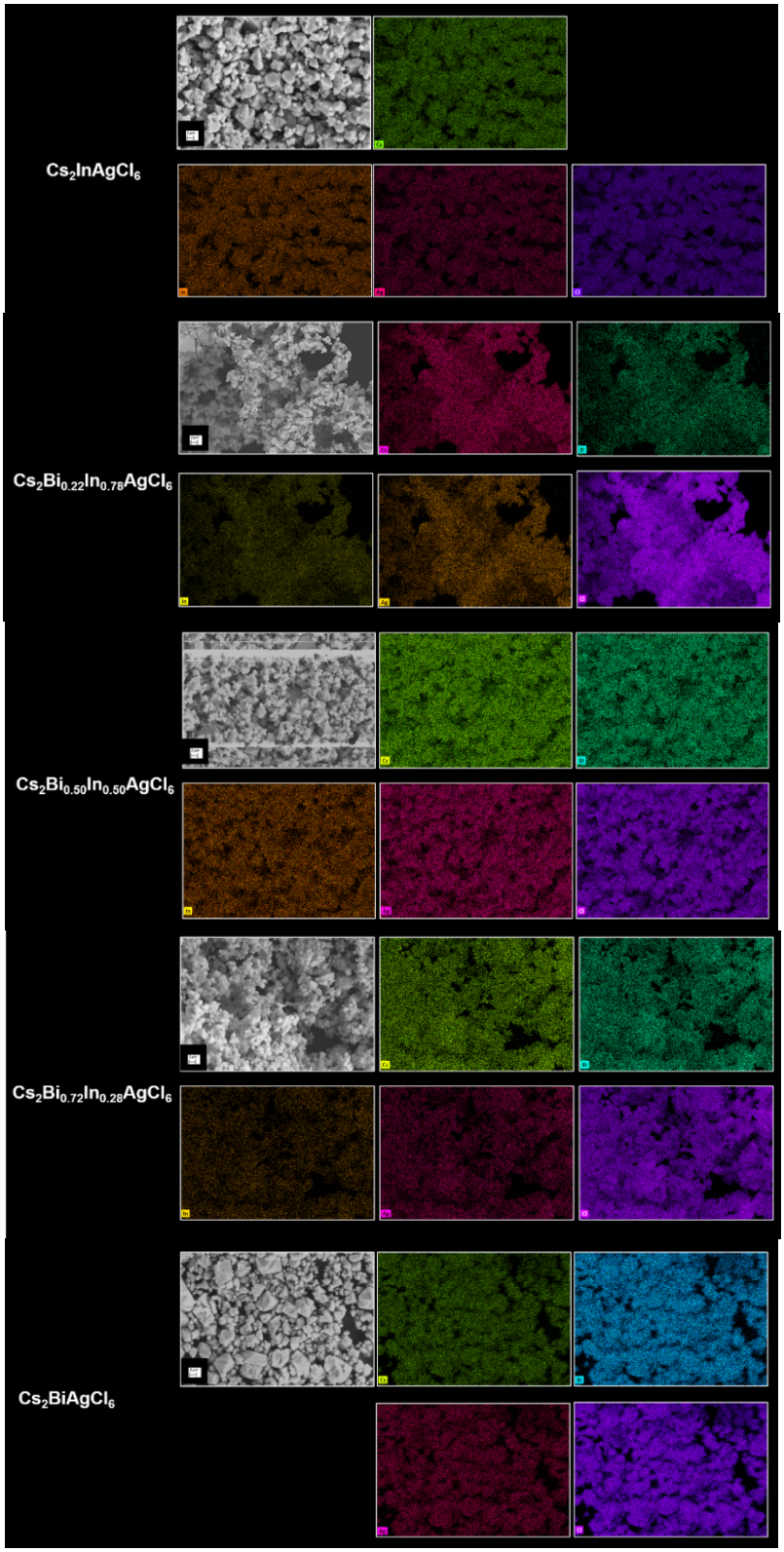

Figure S2. EDS elemental mapping of Cs, Bi, In, Ag, and Cl for $Cs_2Bi_{1-x}In_xAgCl_6$ (top to bottom sequence, x = 1.00, 0.78, 0.50, 0.22, and 0.00).

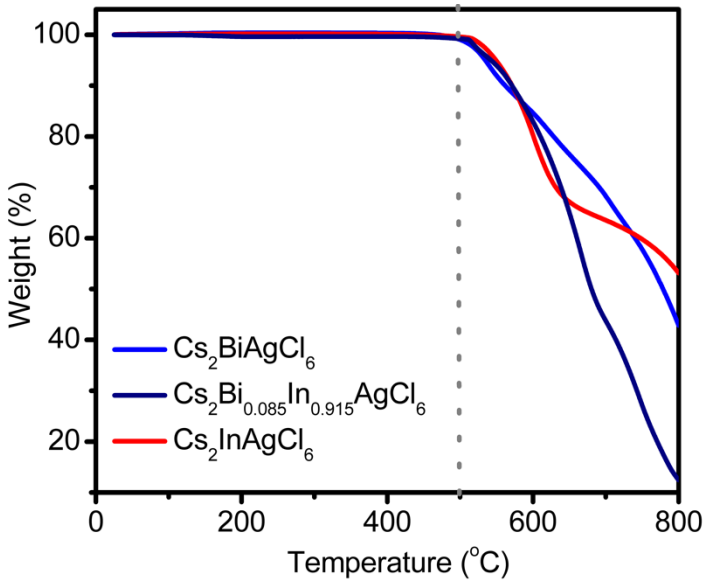

Figure S3. Thermogravimetric analyses (TGA) for $Cs_2BiAgCl_6$, $Cs_2InAgCl_6$, and $Cs_2Bi_{0.085}In_{0.915}AgCl_6$.

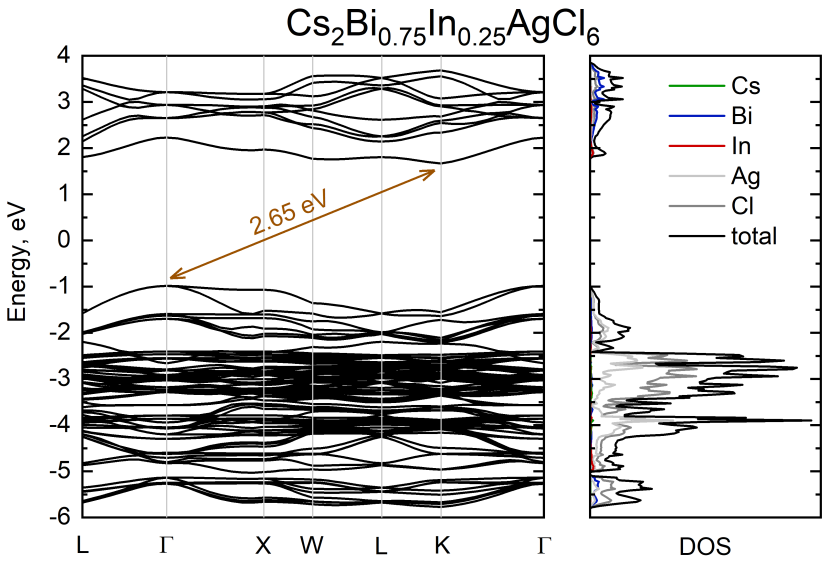

Figure S4. HSE06 DFT band structure and density of states for $Cs_2Bi_{0.75}In_{0.25}AgCl_6$.

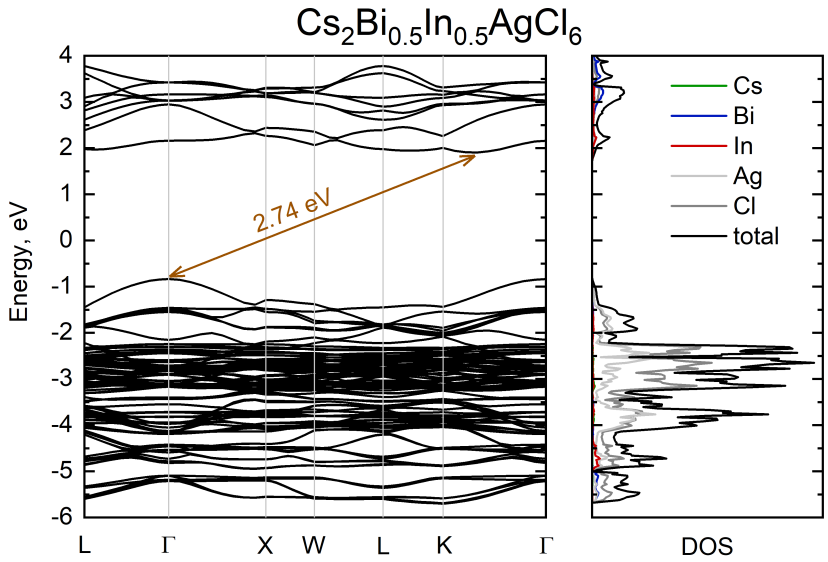

Figure S5. HSE06 DFT band structure and density of states for $Cs_2Bi_{0.5}In_{0.5}AgCl_6$.

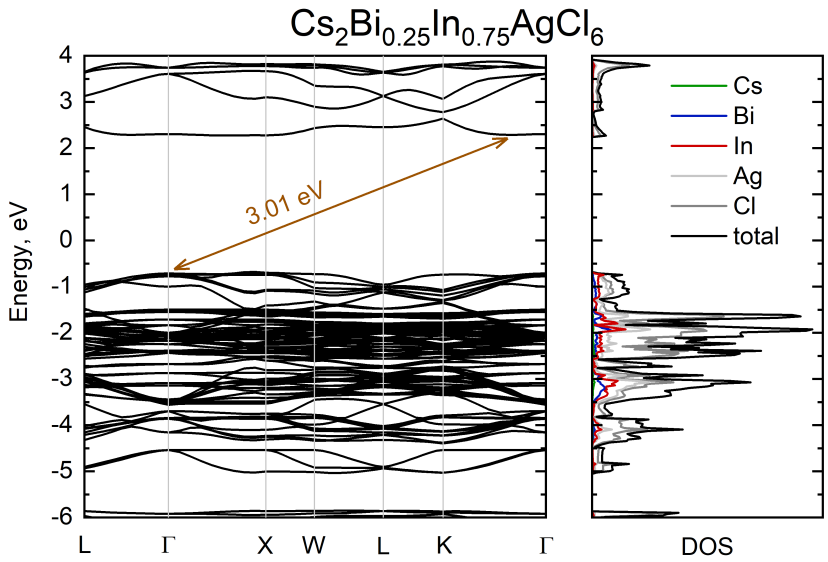

Figure S6. HSE06 DFT band structure and density of states for $Cs_2Bi_{0.25}In_{0.75}AgCl_6$.

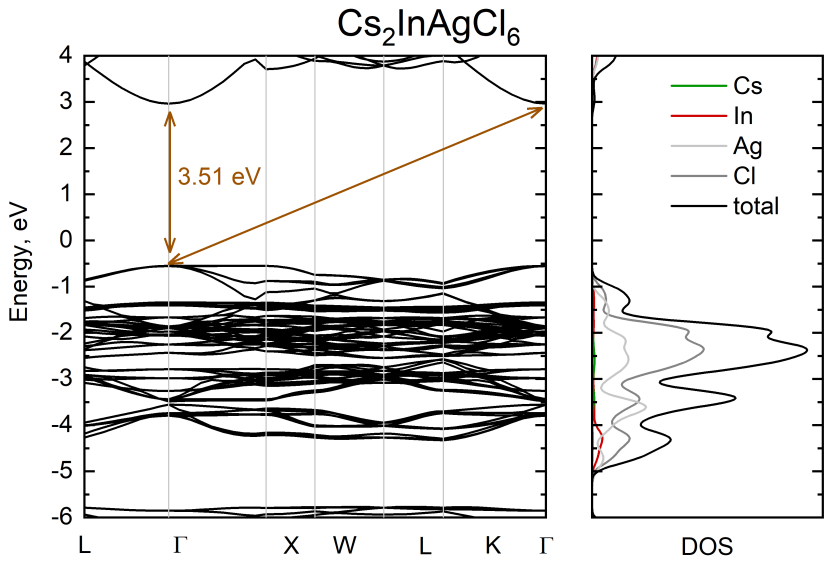

Figure S7. HSE06 DFT band structure and density of states for $Cs_2InAgCl_6$.

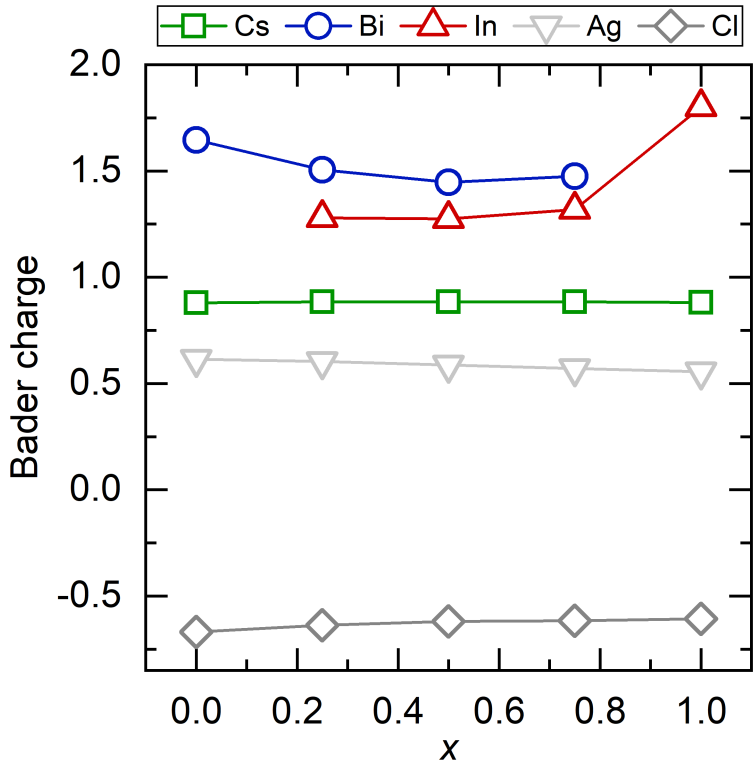

Figure S8. Average Bader charge change in the $Cs_2Bi_{1-x}In_xAgCl_6$ compound series.

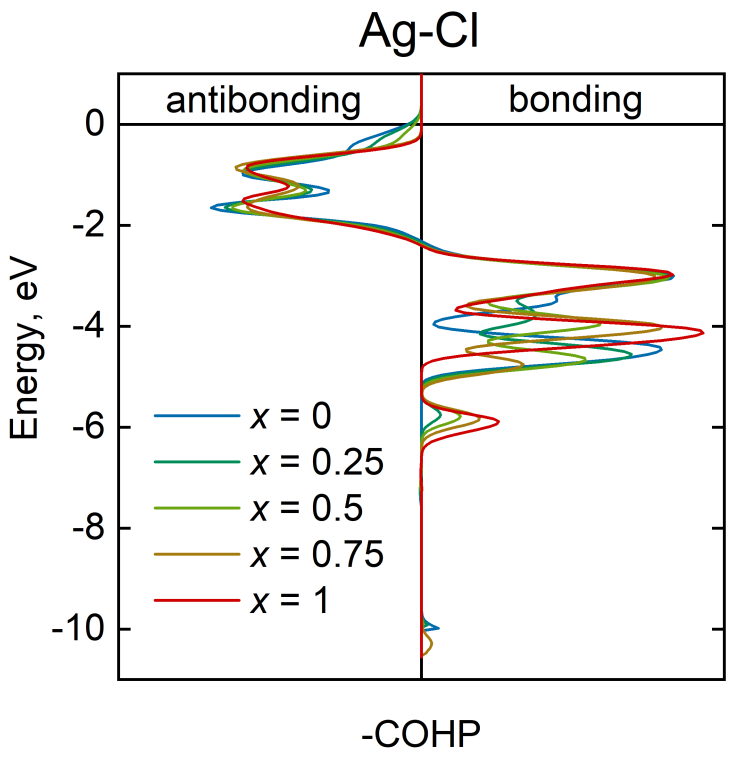

Figure S9. Crystal Orbital Overlap Population (COOP) analysis of the Ag-Cl interactions.

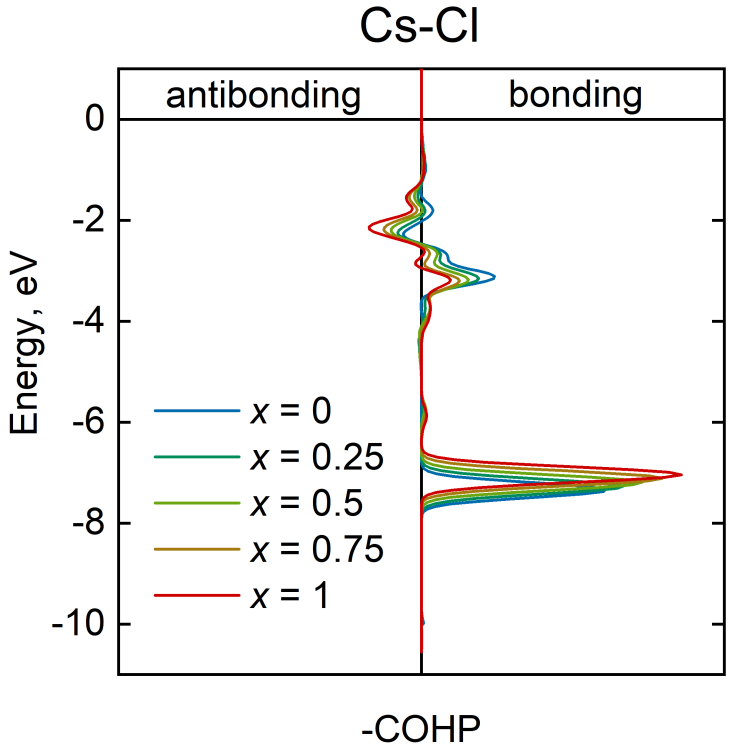

Figure S10. COOP analysis of the Cs-Cl interactions.

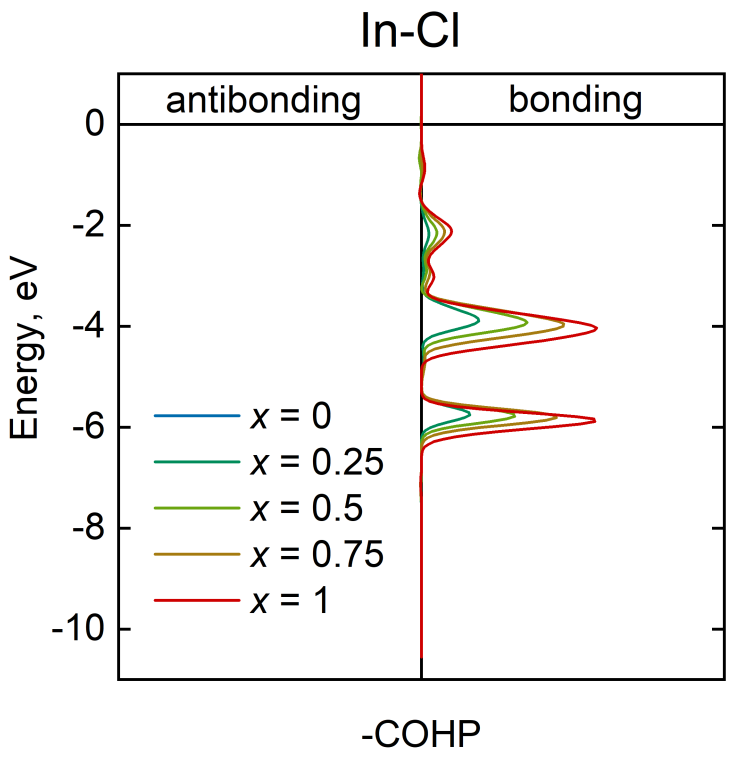

Figure S11. COOP analysis of the In-Cl interactions.

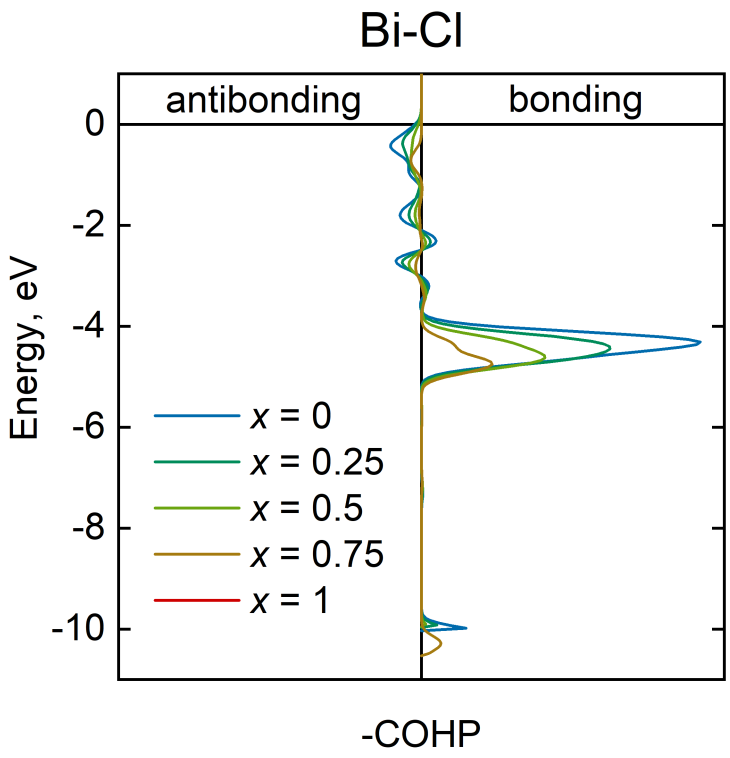

Figure S12. COOP analysis of the Bi-Cl interactions.

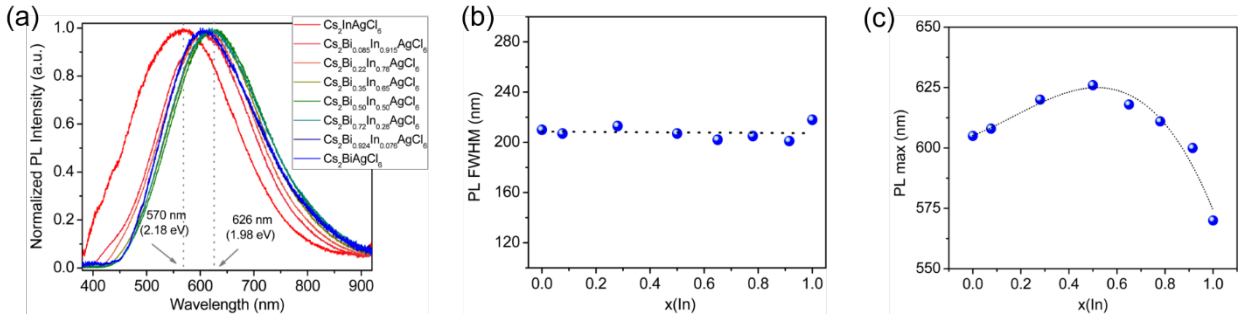

Figure S13. Normalized steady-state PL spectra (a), change in PL FWHM (b), and PL maxima (c) vs indium composition, x(In), in $Cs_2Bi_{1-x}In_xAgCl_6$ ($0 \leq x \leq 1$) HDPs.

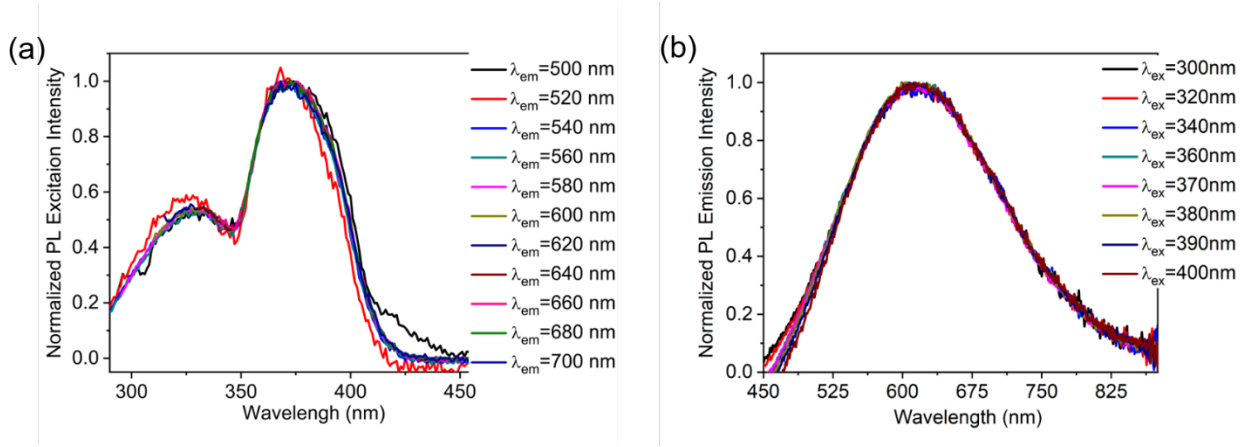

Figure S14. Normalized PL excitation spectra at variable emission wavelengths from 500-700 nm (a), and normalized PL emission spectra with variable excitation wavelengths from 300-400 nm (b) for $Cs_2Bi_{0.085}In_{0.915}AgCl_6$ HDPs.

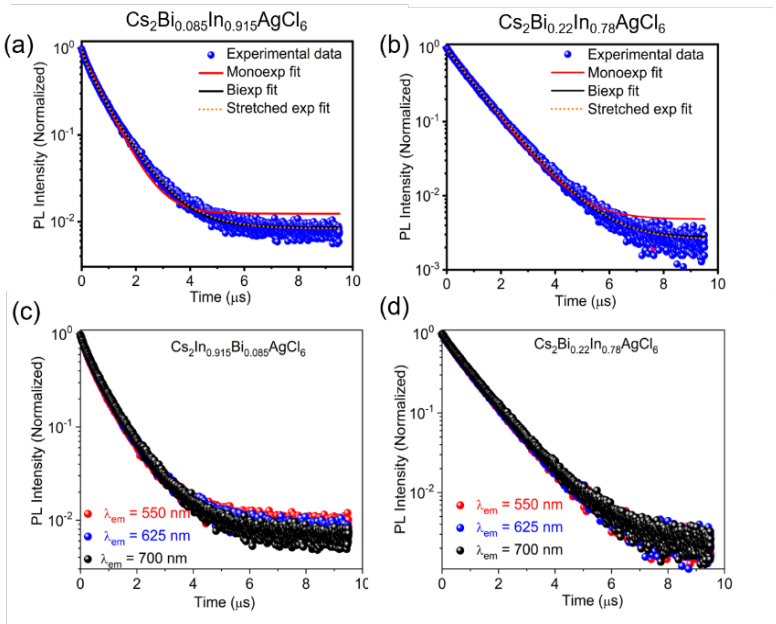

Figure S15. Experimental PL decay with λ_{em} = 625 nm and its monoexponential, biexponential, and stretched-exponential decay fit for $Cs_2Bi_{0.085}In_{0.915}AgCl_6$ (a) and $Cs_2Bi_{0.22}In_{0.78}AgCl_6$ (b) HDPs. Wavelength dependent PL decay plots for $Cs_2Bi_{0.085}In_{0.915}AgCl_6$ (c) and $Cs_2Bi_{0.22}In_{0.78}AgCl_6$ (d) HDPs. Samples were excited using laser excitation at 364 nm.

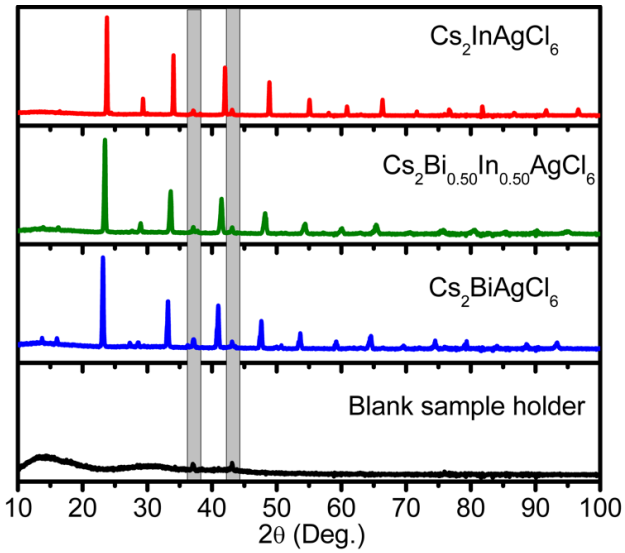

Figure S16. Two background signals (grey highlighted region) appeared in all PXRD patterns at 2θ ~37° and ~ 43° for all $Cs_2Bi_{1-x}In_xAgCl_6$ HDPs. Here, we are showing PXRD of three representative materials (x = 0.00, 0.50, and 1.00) along with the PXRD signals from a blank sample holder.

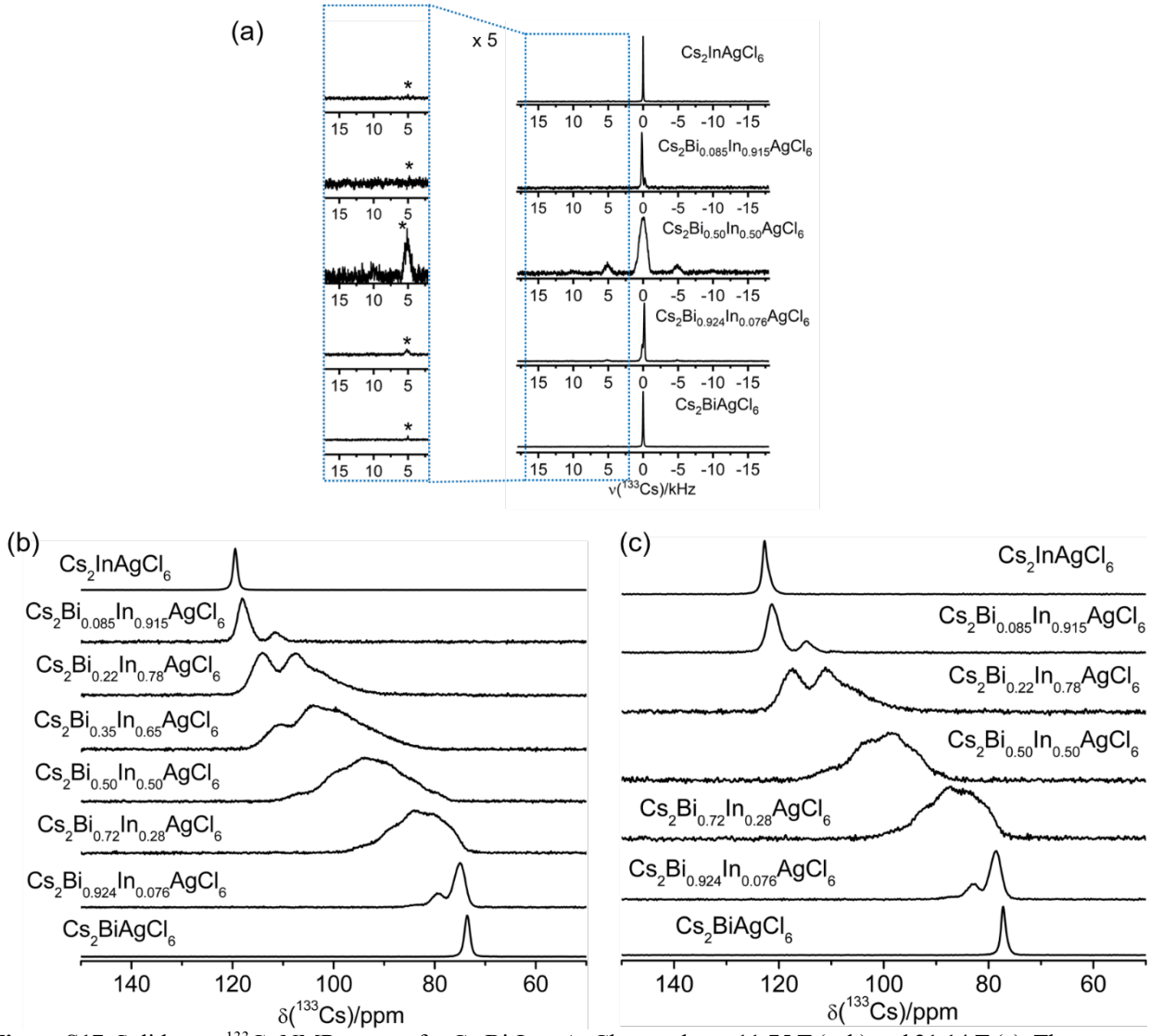

Figure S17. Solid-state ^{133}Cs NMR spectra for $Cs_2Bi_xIn_{1-x}AgCl_6$ samples at 11.75 T (a, b) and 21.14 T (c). The spectra are acquired under magic-angle spinning sample conditions with MAS frequencies of 5 kHz (a), 13 kHz (b) and 30 kHz (c). Spectra are scaled to the same vertical intensity. Please note that the different ^{133}Cs chemical shifts at 11.75 and 21.14 T with magic-angle spinning frequencies of 13 and 30 kHz, respectively, are due to the temperature effect upon magic-angle spinning.[16] The ^{133}Cs NMR peak is shifted towards higher frequencies as the sample temperature is ~12 °C warmer during the measurement (assuming identical ambient conditions, a 4 mm rotor at 13 kHz will add ~ 24 °C vs. ~36 °C for a 2.5 mm rotor at 30 kHz, due to frictional heating).[17]

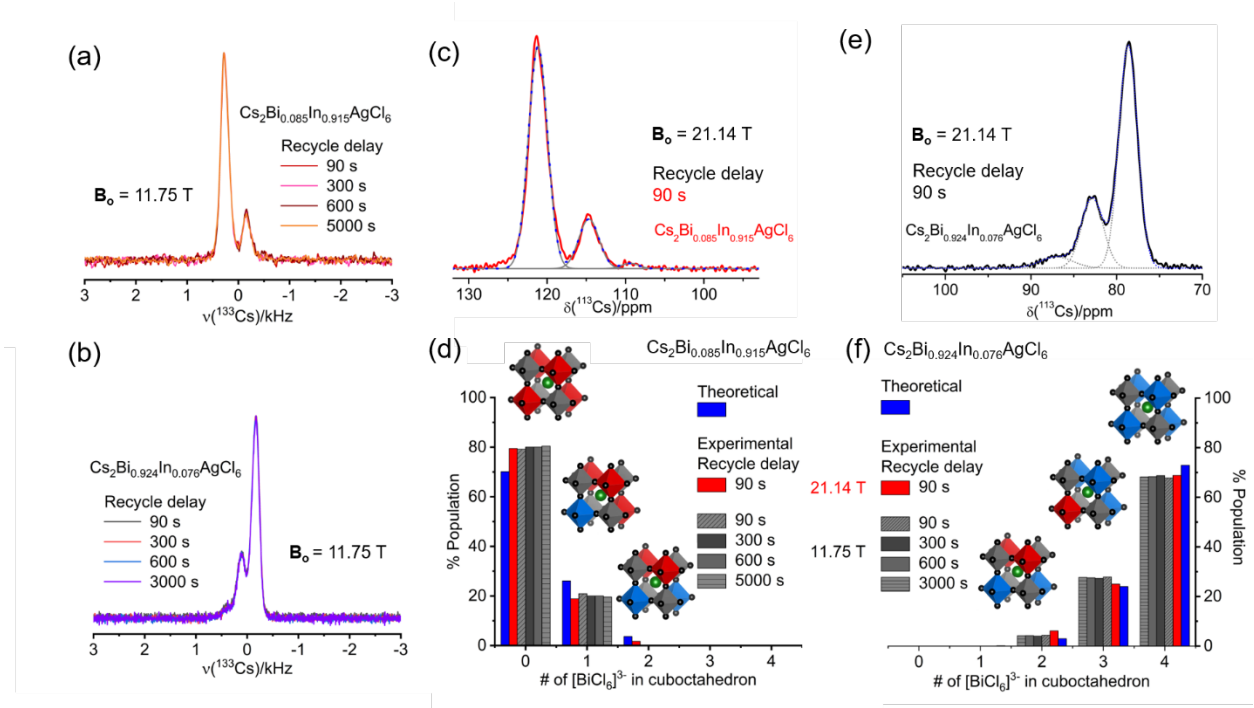

Figure S18. Normalized solid-state ^{133}Cs NMR spectra that are showing spectral overlap of multiple cuboctahedral environments for $Cs_2Bi_{0.085}In_{0.915}AgCl_6$ (a) and $Cs_2Bi_{0.924}In_{0.076}AgCl_6$ (b). The spectra were acquired at 11.75 T with a spinning frequency of 13 kHz and with various recycle delay values as indicated. Gaussian fits of solid-state ^{133}Cs NMR spectra for $Cs_2Bi_{0.085}In_{0.915}AgCl_6$ (c) and $Cs_2Bi_{0.924}In_{0.076}AgCl_6$ (e), acquired at 21.14 T with spinning frequencies of 30 kHz and recycle delay of 90 s. The bar diagrams show the binomial distributions of different ^{133}Cs cuboctahedral sites using Gaussian fits with various recycle delays for $Cs_2Bi_{0.085}In_{0.915}AgCl_6$ (d) and for $Cs_2Bi_{0.924}In_{0.076}AgCl_6$ (f) as indicated.

Supplementary Note 1:

The formula of the binomial distribution is as follows: $P(x) = \frac{n!}{x!(n-x)!} p^x (1-p)^{n-x}$,

where, n and p are the number of trials and the probability of a given trial, respectively.

Here, n = 4, the fraction of bismuth present in B'(III) site is given by p = 0.085 and 0.924 for $Cs_2Bi_{0.085}In_{0.915}AgCl_6$ and $Cs_2Bi_{0.924}In_{0.076}AgCl_6$, respectively, the number of $[BiCl_6]^{4-}$ sites in the cuboctahedron are x = 0, 1, 2, 3, 4.

When, p = 0.085, then the probability P(0) = 70.1%, P(1) = 26.1%, P(2) = 3.6%, P(3) = 0.2% and P(4) = 0.0%.

And when p = 0.924, then P(0) =0.0% , P(1) = 0.2%, P(2) = 2.9% , P(3) = 24.0% and P(4) = 72.9%.

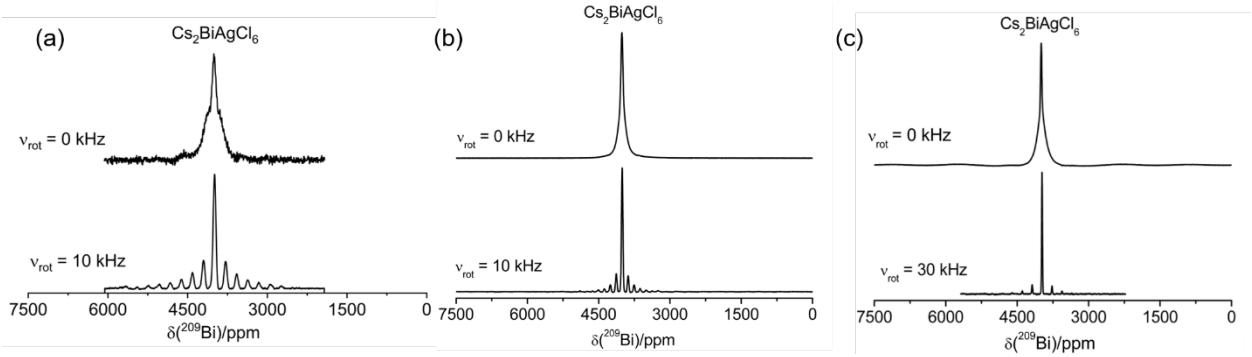

Figure S19. Solid-state ^{209}Bi NMR of $Cs_2BiAgCl_6$ at 7.05 T (a), 11.75 T (b), and 21.14 T (c). The sample was acquired under non-spinning and magic-angle spinning (10 kHz at 7.05 T and 11.75 T, and 30 kHz at 21.14 T) conditions.

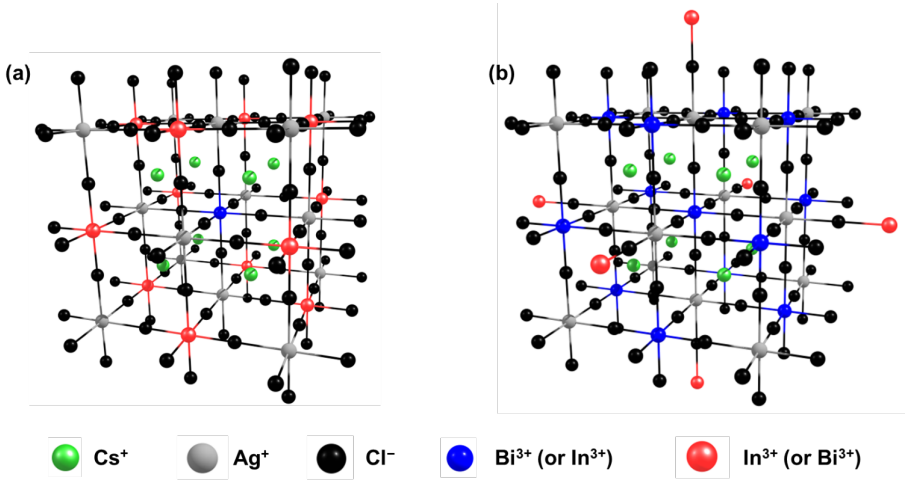

Figure S20. Crystal structures of the mixed In-Bi HDPs, illustrating the 12 possible substitution sites in the first B'(III) coordination sphere (a) and the 6 possible substitution sites in the second B'(III) coordination sphere (b); the substitution atom is shown in red.

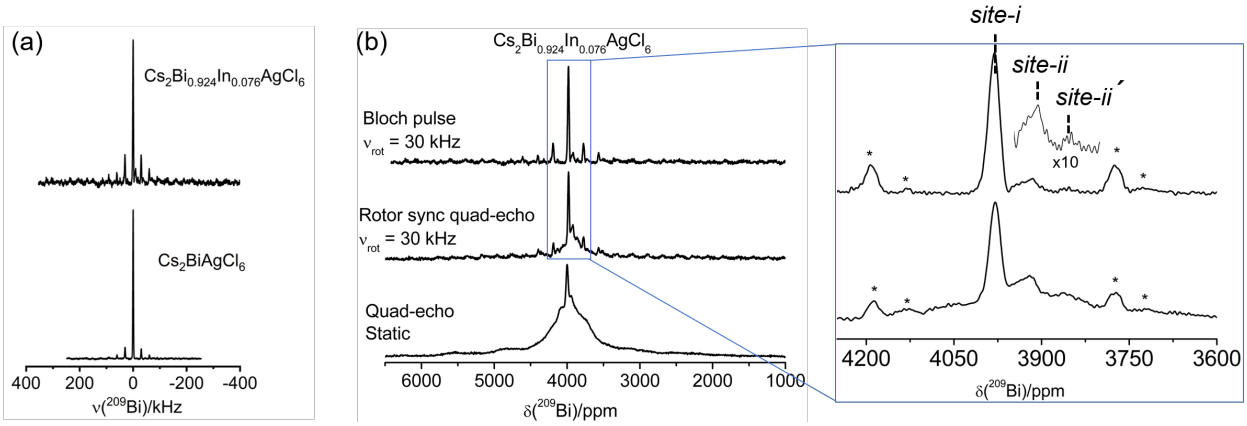

Figure S21. Solid-state ^{209}Bi NMR spectra of $Cs_2BiAgCl_6$ and In^{3+}-doped $Cs_2Bi_{0.924}In_{0.076}AgCl_6$ acquired with a magic angle spinning frequency of 30 kHz at 21.14 T (a). Solid-state ^{209}Bi NMR spectra of $Cs_2Bi_{0.924}In_{0.076}AgCl_6$ acquired under non-spinning and magic-angle spinning (30 kHz) conditions at 21.14 T (b). The ^{209}Bi NMR sites in (b) correspond to distinguishable Bi sites with different medium-range structural environments. The asterisks(∗) in (b) indicate spinning sidebands.

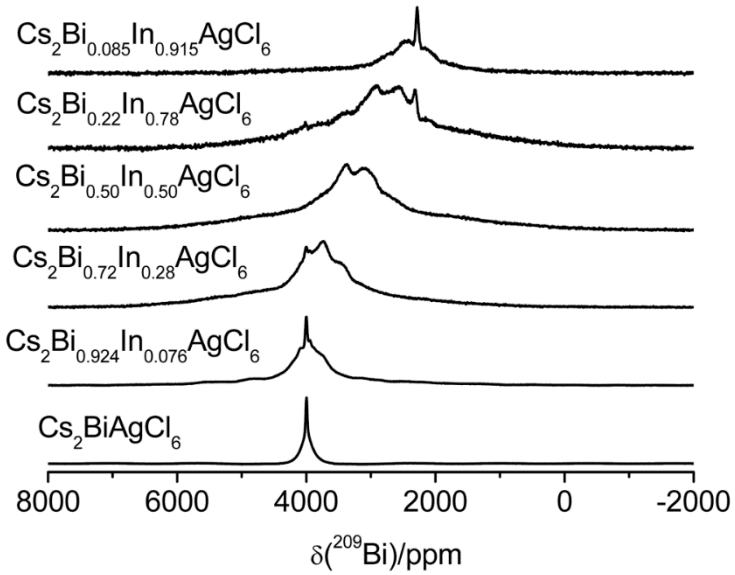

Figure S22. Solid-state ^{209}Bi NMR spectra for $Cs_2Bi_{1-x}In_xAgCl_6$ acquired under non-spinning conditions at 21.14 T. Spectra scaled to the same vertical intensity.

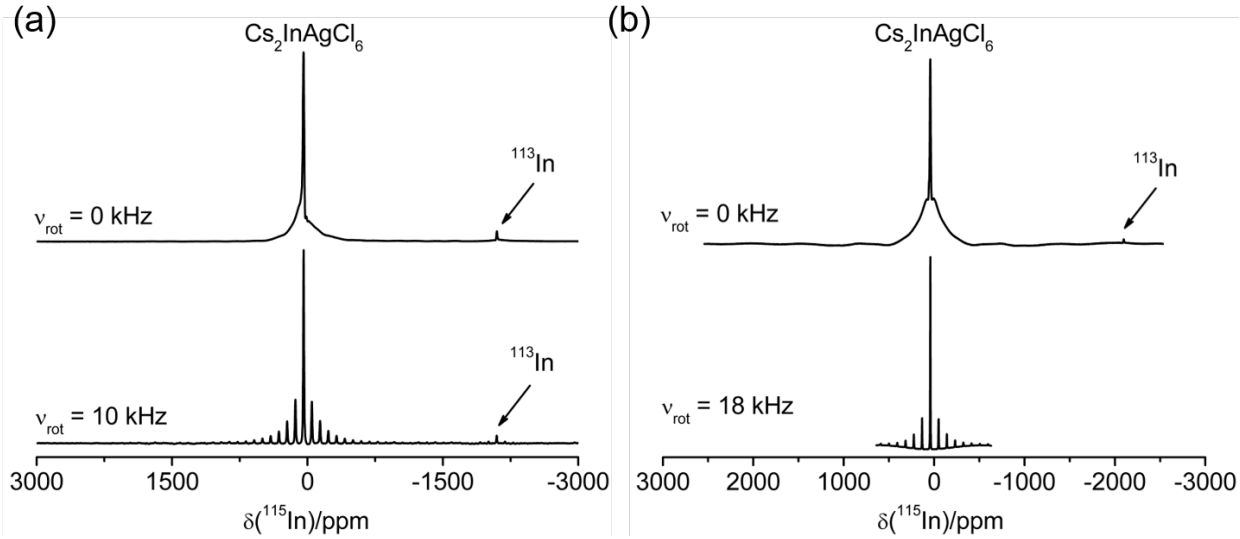

Figure S23. Solid-state ^{115}In NMR spectra of $Cs_2InAgCl_6$ at 11.75 T (a) and 21.14 T (b). The sample was acquired under non-spinning or magic angle spinning conditions as indicated. NB: Spectral width was reduced for acquisition of the MAS NMR spectrum in pane b (bottom).

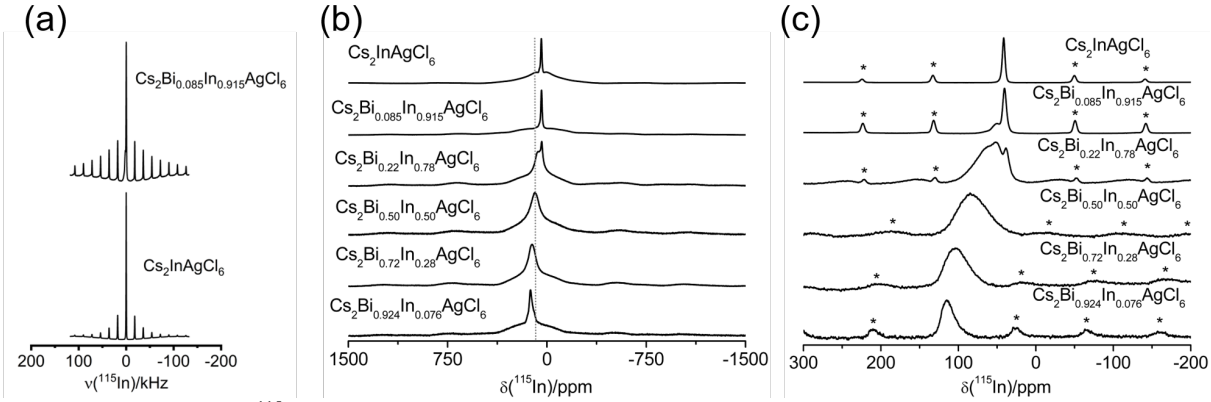

Figure S24. Solid-state ^{115}In NMR spectra of $Cs_2InAgCl_6$ and $Cs_2Bi_{0.085}In_{0.915}AgCl_6$ acquired with a spinning frequency of 18 kHz at 21.14 T (a). Solid-state ^{115}In NMR spectra of non-spinning (b) and of magic angle spinning (18 kHz, c) samples of $Cs_2Bi_{1-x}In_xAgCl_6$ acquired at 21.14 T. The asterisks (∗) in (c) indicate spinning sidebands. Spectra scaled to the same vertical intensity.

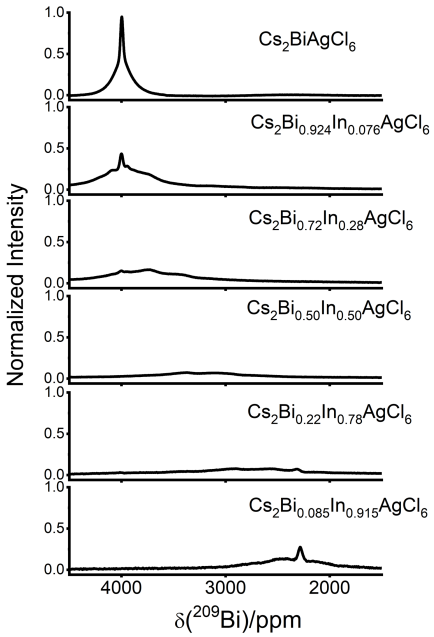

Figure S25. Normalized intensities of ^{209}Bi NMR spectra for non-spinning $Cs_2Bi_{1-x}In_xAgCl_6$ samples. The normalization signifies that the intensity is vertically scaled to the same amount of Bi in the sample for a given number of scans.

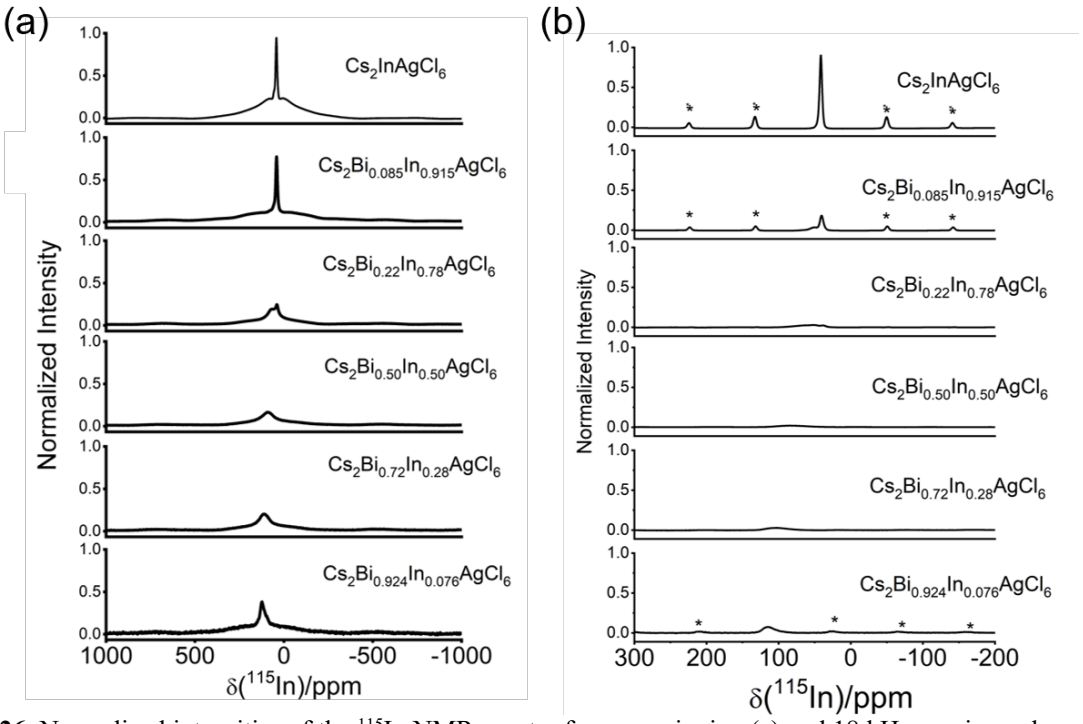

Figure S26. Normalized intensities of the ^{115}In NMR spectra for non-spinning (a) and 18 kHz magic-angle spinning (b) $Cs_2Bi_{1-x}In_xAgCl_6$ samples as indicated. The asterisks (∗) in (b) indicate spinning sidebands. The normalization signifies that the intensity is vertically scaled to the same amount of In in the sample for a given number of scans.

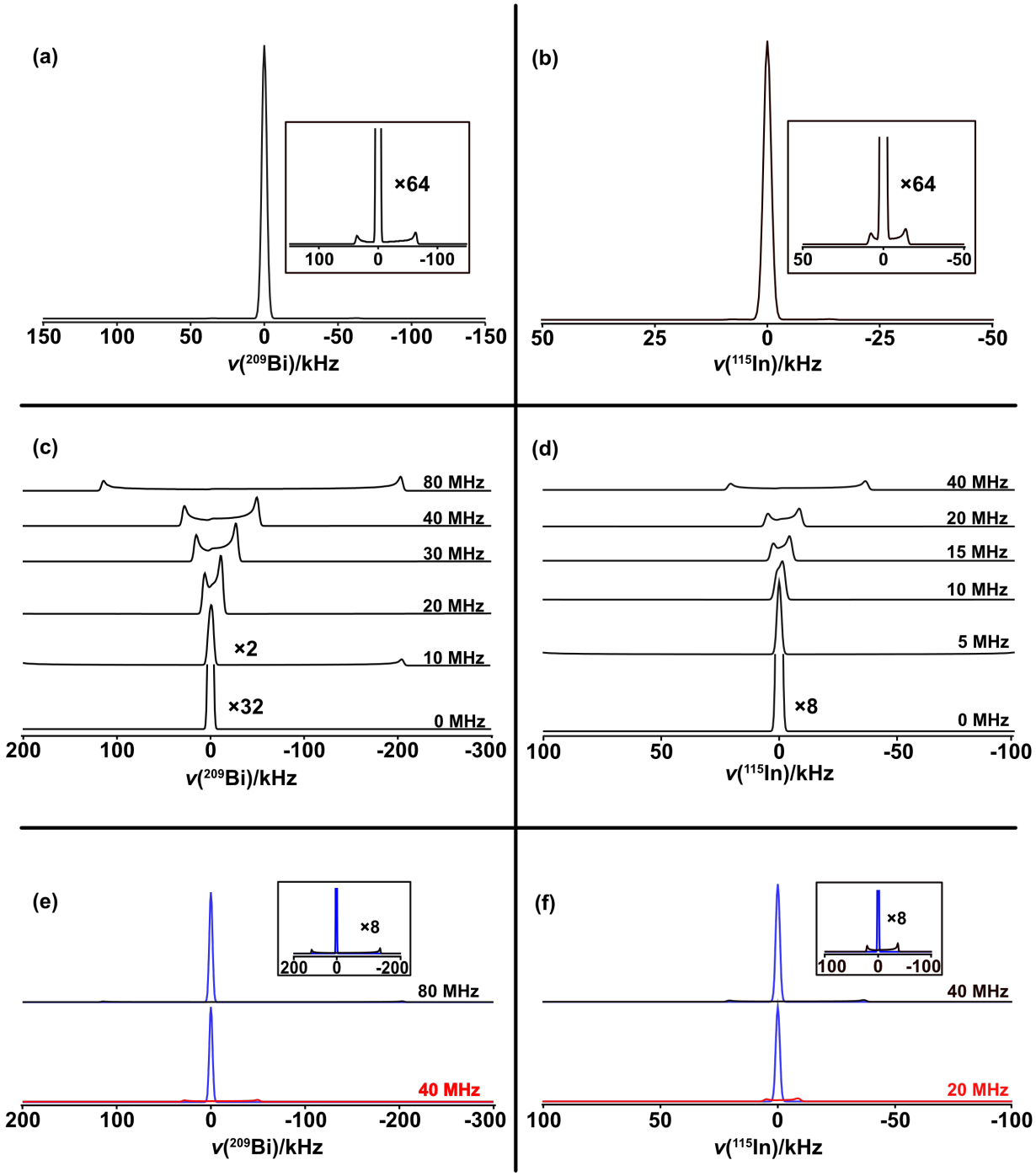

Figure S27. Simulated ^{209}Bi (a) and ^{115}In (b) NMR spectra expected for spectra acquired at 21.14 T assuming a two site model, with C_Q = 0 and 45 MHz (^{209}Bi) or 0 and 25 MHz (^{115}In); both spectra were simulated assuming 90 % of the sites were those with no quadrupolar interaction. In (c) and (d), ^{209}Bi and ^{115}In NMR spectra, simulated with the indicated C_Q at 21.14 T, illustrate the relative impact of C_Q on the intensity of that peak, assuming an equal probability for a given NMR site. The peak at −200 kHz and C_Q = 10 MHz in (c) is due to the signal expected for the 3/2 – ½ transition. In (e) and (f), Spectra with the indicated quadrupolar coupling, shown in red and black, are overlain with those for the nucleus with C_Q = 0, shown in blue; the simulations assumed equal probabilities for the two sites in the spectra shown in (e) and (f).

REFERENCES:

(1) Kubelka, P.; Munk, F. Ein Beitrag Zur Optik Der Farbanstriche. *Z.Tech. Phys. (Leipzig)* **1931**, *12*, 593–601.

(2) J. H. Davis; K. R. Jeffrey; M. Bloom; M. I. Valic; T. P. Higgs. Quadrupolar Echo Deuteron Magnetic Resonance Spectroscopy in Ordered Hydrocarbon Chains. *Chem. Phys. Lett.* **1976**, *42*, 390–394.

(3) Bodart, P. R.; Amoureux, J.-P.; Dumazy, Y.; Lefort, R. Theoretical and Experimental Study of Quadrupolar Echoes for Half-Integer Spins in Static Solid-State NMR. *Mol. Phys.* **2000**, *98*, 1545–1551.

(4) Kohout, M.; Wagner, F. R.; Grin, Y. Electron Localization Function for Transition-Metal Compounds. *Theor. Chem. Acc.* **2002**, *108*, 150–156.

(5) Grin, Y.; Savin, A.; Silvi, B. The ELF Perspective of Chemical Bonding. In *Wiley-VCH Verlag GmbH & Co. KGaA: Weinheim, Germany*; 2014; 345–382.

(6) Kohout, M.; Savin, A. Influence of Core**.**Valence Separation of Electron Localization Function. *J. Comput. Chem.* **1997**, *18*, 1431–1439.

(7) Rezende, M. V. d. S. .; Araujo, R. M. .; Valerio, M. E. G. .; Jackson, R. A. Intrinsic Defects in Strontium Aluminates Studied via Computer Simulation Technique. *J. Phys. Conf. Ser.* **2010**, *249*, 012042.

(8) Kresse, G.; Joubert, D. From Ultrasoft Pseudopotentials to the Projector Augmented-Wave Method. *Phys. Rev. B Condens. Matter Mater. Phys.* **1999**, *59*, 1758−1775.

(9) Kresse, G.; Furthmuller, J. Efficient Iterative Schemes for Ab Initio Total-Energy Calculations Using a Plane-Wave Basis Set. *Phys. Rev. B Condens. Matter Mater. Phys.* **1996**, *54*, 11169−11186.

(10) Tang, W.; Sanville, E.; Henkelman, G. A Grid-Based Bader Analysis Algorithm without Lattice Bias. *J. Phys. Condens. Matter* **2009**, *21*, 084204.

(11) Clark, S. J.; Segall, M. D.; Pickard, C. J.; Hasnip, P. J.; Probert, M. I. J.; Refson, K.; Payne, M. C. First Principles Methods Using CASTEP. *Z. Krist. - Cryst. Mater* **2005**, *220*, 567–570.

(12) Perdew, J. P.; Burke, K.; Ernzerhof, M. Generalized Gradient Approximation Made Simple. *Phys. Rev. Lett.* **1996**, *77*, 3865–3868.

(13) Perdew, J. P. .; Burke, K. .; Ernzerhof, M. Perdew, Burke, and Ernzerhof Reply. *Phys. Rev. Lett.* **1998**, *80*, 891.

(14) Yates, J. R.; Pickard, C. J.; Mauri, F. Calculation of NMR Chemical Shifts for Extended Systems Using Ultrasoft Pseudopotentials. *Phys. Rev. B* **2007**, *76*, 024401.

(15) Harris, R. K.; Becker, E. D. NMR Nomenclature: Nuclear Spin Properties and Conventions for Chemical Shifts—IUPAC Recommendations. *J. Magn. Reson.* **2002**, *156*, 323–326.

(16) Karmakar, A.; Dodd, M. S.; Agnihotri, S.; Ravera, E.; Michaelis, V. K. Cu(II)-Doped $Cs_2SbAgCl_6$ Double Perovskite: A Lead-Free, Low-Bandgap Material. *Chem. Mater.* **2018**, *30*, 8280–8290. h

(17) Bernard, G. M.; Goyal, A.; Miskolzie, M.; McKay, R.; Wu, Q.; Wasylishen, R. E.; Michaelis, V. K. Methylammonium Lead Chloride: A Sensitive Sample for an Accurate NMR Thermometer. *J. Magn. Reson.* **2017**, *283*, 14–21.